Viewpoint

Neuron

Can One Concurrently Record Electrical Spikes from Every Neuron in a Mammalian Brain?

Highlights

- Physical limits do not preclude simultaneous recordings of all spikes in neocortex
- Future electrodes need nontraditional materials and fabrication procedures
- Challenges for dense recording include heat dissipation from interface electronics

Authors

David Kleinfeld, Lan Luan, Partha P. Mitra, Jacob T. Robinson, Rahul Sarpeshkar, Kenneth Shepard, Chong Xie, Timothy D. Harris

Correspondence

dk@physics.ucsd.edu (D.K.), harrist@janelia.hhmi.org (T.D.H.)

In Brief

Understanding cognition can, in principle, require simultaneous records of spikes from every neuron in cortex. Can this be achieved? The results from back-of-the-envelope calculations show that such measurements may be obtained using electrodes fabricated with existing yet nontraditional materials and procedures.

Kleinfeld et al., 2019, Neuron *103*, 1–11
September 25, 2019
https://doi.org/10.1016/j.neuron.2019.08.011

CellPress

Please cite this article in press as: Kleinfeld et al., Can One Concurrently Record Electrical Spikes from Every Neuron in a Mammalian Brain?, Neuron (2019), https://doi.org/10.1016/j.neuron.2019.08.011

Neuron
Viewpoint

CellPress

Can One Concurrently Record Electrical Spikes from Every Neuron in a Mammalian Brain?

David Kleinfeld,[1,2,13,*] Lan Luan,[3] Partha P. Mitra,[4] Jacob T. Robinson,[5] Rahul Sarpeshkar,[6,7,8,9] Kenneth Shepard,[10] Chong Xie,[3] and Timothy D. Harris[11,12,*]
[1]Section of Neurobiology, University of California, San Diego, CA, USA
[2]Department of Physics, University of California, San Diego, CA, USA
[3]Department of Biomedical Engineering, University of Texas, Austin, TX, USA
[4]Cold Spring Harbor Laboratory, Cold Spring Harbor, NY, USA
[5]Department of Electrical and Computer Engineering, Rice University, Houston, TX, USA
[6]Department of Engineering, Dartmouth, Hanover, NH, USA
[7]Department of Microbiology and Immunology, Dartmouth, Hanover, NH, USA
[8]Department of Molecular and Systems Biology, Dartmouth, Hanover, NH, USA
[9]Department of Physics, Dartmouth, Hanover, NH, USA
[10]Department of Electrical Engineering, Columbia University, New York, NY, USA
[11]Howard Hughes Medical Institutes, Janelia Research Campus, Ashburn, VA, USA
[12]Department of Bioengineering, Johns Hopkins University, Baltimore, MD, USA
[13]Lead Contact
*Correspondence: dk@physics.ucsd.edu (D.K.), harrist@janelia.hhmi.org (T.D.H.)
https://doi.org/10.1016/j.neuron.2019.08.011

SUMMARY

The classic approach to measure the spiking response of neurons involves the use of metal electrodes to record extracellular potentials. Starting over 60 years ago with a single recording site, this technology now extends to ever larger numbers and densities of sites. We argue, based on the mechanical and electrical properties of existing materials, estimates of signal-to-noise ratios, assumptions regarding extracellular space in the brain, and estimates of heat generation by the electronic interface, that it should be possible to fabricate rigid electrodes to concurrently record from essentially every neuron in the cortical mantle. This will involve fabrication with existing yet nontraditional materials and procedures. We further emphasize the need to advance materials for improved flexible electrodes as an essential advance to record from neurons in brainstem and spinal cord in moving animals.

INTRODUCTION

Electrical recordings are the *sine qua non* for the measurement of computations in the nervous system. It is thus of fundamental interest to ask if, as a matter of principle, one can record spikes from all neurons in a mammalian brain. And, if not, from what fraction of the brain can one record? In this regard, the discussions that led to the United States BRAIN Initiative were convened with a working title of The Brain Activity Map (Alivisatos et al., 2012). The prospects for such a dynamic map (Buzsáki et al., 2015), with a corresponding connectome (Denk and Horstmann, 2004) to map all chemical and resistive connections among neurons, forms the basis for modeling and ultimately understanding brain function (Kleinfeld et al., 2011; Plaza et al., 2014; Rubinov et al., 2015). Here we discuss the physical limits to obtain the brain-wide activity map in a mammal. The corresponding connectivity map could be obtained via transmission electron microscopy (Kasthuri et al., 2015) or focused ion beam milling combined with scanning electron microscopy (Knott et al., 2008; Hayworth et al., 2019). As demonstrated for nonmammalian species (Kornfeld and Denk, 2018), there are no fundamental barriers beyond the constraints of experimental time and the current need for substantial human curating.

Both optical and electrical approaches have been taken to measure neuronal activity across many sites, albeit the most pervasive is optical imaging using a fluorescent indicator of intracellular Ca^{2+} concentration (Grienberger and Konnerth, 2012). While no doubt useful, $[Ca^{2+}]$ transients are only an approximate reflection of spiking (Theis et al., 2016). The advent of genetically expressible voltage sensors may obviate this problem (Platisa and Pieribone, 2018). Yet currently available sensors, while impressive for recording local network activity *in vivo* (Adam et al., 2019; Abdelfattah et al., 2019), appear insufficiently sensitive for brain-wide imaging and require sparsely labeled brain regions to prevent cross-talk from obfuscating the desired signals. Lastly, the photon budget to simultaneously image large numbers of neurons and the technology to image at all depths throughout cortex without deleterious aberrations (Ji, 2017; Liu et al., 2019) remain an elusive goal. Our focus here is on a classical approach, that of measuring extracellular electrical potentials (Lemon, 1984). These signals depend on current flow through the extracellular space during the propagation of an action potential. While the signal-to-noise ratio can be quite high, it is important to recall that isopotential neurons, e.g., electrically compact cells, will not generate an extracellular signal (Jack et al., 1974). This contingency, however, seems unlikely to apply to neurons that are present in neocortex.

A corollary of our query is that of sufficiency. That is, from what fraction of all cells does one need to record to determine how few neurons are needed to quantize the neuronal basis of perception or behavior? This question is bound up in the issue of the dimensionality of neuronal computations (Ganguli and Sompolinsky, 2012; Gao et al., 2017; Stringer et al., 2019), i.e., how fine a sensory field is perceived, or how finely controlled is motion within a motor act? Further, the question of sufficiency is likely to be widely variable for different parts of the brain (Lehky et al., 2014; Schölvinck et al., 2015). Thus we focus on the reductionist issue of fundamental physical limits, practical limits, and numbers.

Theory, together with transport and mechanical parameters for known materials, places physical limits on the dimensions of wires. For example, how stiff does an electrode shank need to be before it buckles in the insertion process? What force is required to insert a probe of a given cross-section? How thick a wire does one require to propagate a signal without appreciable attenuation at action potential frequencies? For concreteness, we discuss a cylindrical probe of diameter d_{shaft} with recording sites distributed along the length of the shank. We consider the case of neocortex with dimensions appropriate for mouse through marmoset. We ask if, in principle, enough multi-electrode shanks could be inserted into the cortex to reliably record spikes from all neurons. Conversely, if we set an upper limit for displaced brain tissue, this same calculation can be used to estimate the fraction of neurons whose spiking could be detected with available probes.

We first establish the essential parameters for the electrical measurement process. We then consider physical arguments for the size and density of electrode carriers and electrodes that will enable electrical recordings with high signal-to-noise ratios. Lastly, we discuss potential physiological constraints, including the thermal load from the associated electronics.

RESULTS

Neuroelectric Scales

The electrical capture length for extracellular recording from a neuron, denoted D, is key. The average density of neurons in murine cortex is $\rho = 1 \times 10^5/\text{mm}^3$ (Petersen, 2007; Tsai et al., 2009), which roughly translates to a cube that is $\rho^{1/3} \approx 20$ μm on edge per neuron. The range of extracellular spike detection is an issue of signal amplitude relative to that of background spiking activity. While detection of spikes more than 100 μm from the originating soma has been demonstrated for the largest cortical pyramidal neurons (Buzsáki, 2004), the detection length is less well defined for smaller neurons. A conservative estimate of the range of detection is the electronic length for a propagating action potential. This length is set by the ratio of current flow through the membrane, which is dominated by sodium conductance during an action potential, to current flow that is along the axis of the axon (Jack et al., 1974). Typically, $\lambda_{AP} \approx 20$ μm, which matches the neuronal spacing $\rho^{1/3} \approx 20$ μm. Thus we take $D = 20$ μm as the maximum length between a neuron and an electrode for reliable recording. Clearly, there are significant variations in neuronal size, and D will depend on cell geometry and levels of channel expression.

The second scale is the bandwidth of neuronal signaling, which we denote as f_{AP}. The spectral density of the action potential extends to 10 kHz (Fee et al., 1996), so that we assign $f_{\text{AP}} = 10$ kHz. We note in passing that the collective activation of sodium channels in the axon hillock has spectral components up 40 kHz (Naundorf et al., 2006), yet the components above 10 kHz are not essential to the detection of a spike.

Metrology

What is the minimum distance between electrode shanks? We put the issue of displacement of brain tissue by the electrodes aside for the moment. Ideally, the shanks should be spaced at nominally $2D \approx 40$ μm, so that each neuron is, on average, within one electronic length of a shank. The shanks are chosen to be arranged in a triangular array with a spacing of $2D = 40$ μm (Figure 1A).

With the above parameters for detection range and bandwidth, we can estimate limits to the diameter of the electrode shank. This shank should cause the smallest feasible tissue displacement, contain recording sites of sufficient density to resolve the signals from the full density of neurons, and have a mechanical strength sufficient to insert into cortex.

Design Considerations for Rigid Probes

We now estimate the diameter of our canonical shank. With additional information, we can further estimate the number and size of the electrode pads and leads.

A critical limit for the fabrication of the thinnest usable rigid probe is the buckling force at the time of insertion of the electrode into cortex. This constrains the dimensions of the shank. The ideal material for a rigid shank, i.e., the stiffest and thus most resistant to buckling, is diamond, with Young's modulus $E = 1.2$ N/μm^2. By comparison, $E = 0.2$ N/μm^2 for silicon. We choose a recording depth of $L_{shaft} = 2000$ μm, which is appropriate for mouse through marmoset cortex. Recent measurements of the force required to insert cylindrical electrodes into mouse cortex, *ex vivo*, with diameters ranging from 7.5 to 100 μm, yield a penetration force of $F_i = F_0\ (1 + d/d_0)$, with $F_0 = 8 \times 10^{-6}$ N and $d_0 = 1$ μm (Obaid et al., 2018). Note that the penetration force reported for a 100 μm diameter probe is about 6 times less than that was reported for inserting electrodes in monkey cortex (Reitboeck, 1983). Lastly, the sustaining force to insert the electrode did not exceed the penetrating force down to at least 1,500 μm of insertion depth (Obaid et al., 2018).

Our dimensional estimates (Box 1) for diamond shanks supports the use of cylindrical electrodes that are at least 4 μm in diameter. We choose the larger value of $d_{\text{shaft}} = 6$ μm, based on electrical considerations (Box 2), for which the volume fraction of the brain occupied by the electrodes, denoted Θ, is $\Theta \approx 0.02$. This value for the volume fraction is tenfold less than the mean extracellular volume fraction (Tønnesen et al., 2018).

The mechanical and electrical properties of currently available materials allow, in principle, for spikes to be recorded from all neurons in a slab equivalent to that of the cortical mantle of mouse or marmoset (Boxes 1 and 2). The proposed design, constrained by neuronal density and the extracellular volume, consists of electrode shafts arranged on a triangular lattice, spaced

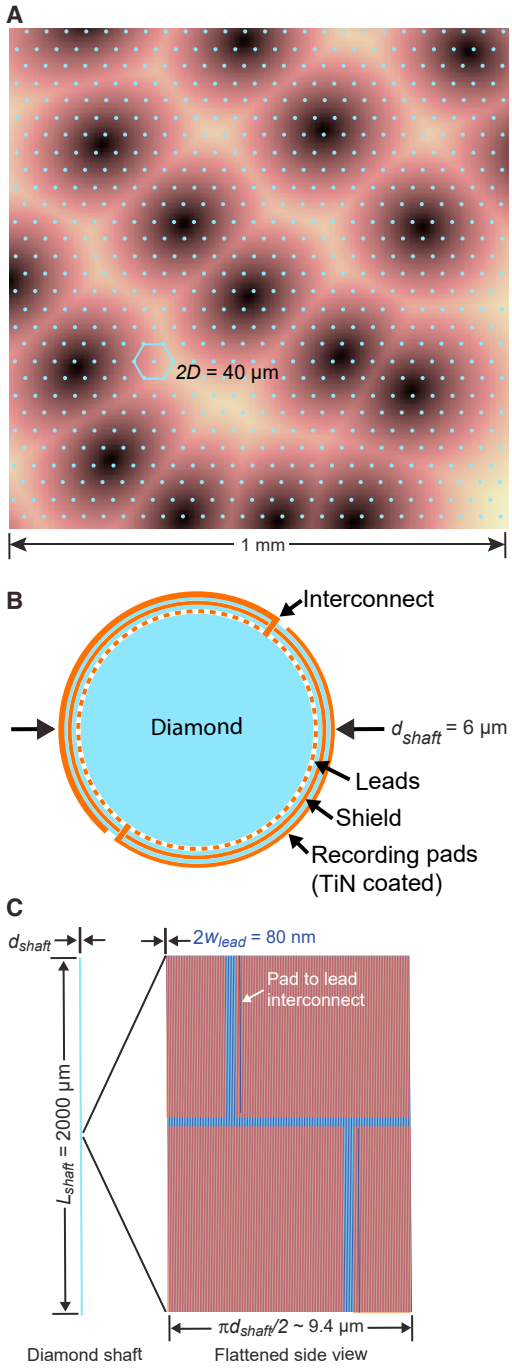

Figure 1. Schematic of the Proposed Stiff Electrode

(A) The proposed triangular grid of electrodes spaced on top of primary vibrissa sensory cortex. Image from Knutsen et al. (2016).

(B) The electrode is constructed of a diamond shaft that is covered with five layers. First is the leads and the mineral insulation between leads, second is mineral insulation, third is a conducting shield, fourth is a second mineral insulation layer, and fifth is the electrode pads. Each pad is connected to one lead via a thru-hole interconnect that pierces the shield. Illustration is not to scale.

(C) The multi-electrode shaft with an expanded view of the face to show the arrangement of pads.

$2D$ = 40 μm. Each multi-site electrode shaft has 280 pads, 9 μm in width with a 14 μm pitch, on a shaft that is 6 μm in diameter and 2000 μm in length. The pads are joined to insulated leads by thru-hole interconnects. We next ask if the geometry and size of the electrodes are consistent with signal-to-noise and bandwidth constraints for the detection of neuronal spikes.

The estimated RMS noise, which is dominated by the thermal noise of the electrode pad, is $\sqrt{\delta V_{pad}^2 + \delta V_{lead}^2 + \delta V_{tissue}^2} \approx 6$ μV. Thus the estimated peak signal-to-RMS-noise ratio of the probe should exceed 50:1 for an action potential amplitude of ΔV_{meas} = 300 μV. Note that the measured fluctuations in vivo will further contain nonstationary contributions from active sources, including spiking by distant neurons and other fast ionic processes. A RMS value of δV_{RMS} = 25 μV was reported for regularly spiking neurons in primary vibrissa cortex (Fee et al., 1996). Including these physiological sources, the estimated signal-to-RMS-noise ratio of the probe drops to 12:1.

Our estimates are conservative. The minimum diameter of the electrode required to forestall buckling may be reduced by sharpening the electrode tip (Obaid et al., 2018). Further, a guide tube may be used to reduce the unsupported length of the electrode. Past work also suggests the utility of dissolvable supports (Weltman et al., 2016) and microfluidic injection systems (Vitale et al., 2018). Lastly, the noise of the implanted electrode pads will decrease with improvements in the stability of coatings. In addition to TiN, poly(3,4-ethylenedioxythiophene (PEDOT) (Charkhkar et al., 2016; Ludwig et al., 2011; Rivnay et al., 2015), sputtered Pt (Whalen et al., 2006), and IrOx (Negi et al., 2010) are other materials to consider.

Comparison with the State-of-the-Art Rigid Probes

The status of current high-density density probes was reviewed by Steinmetz, Koch, Harris and Caradini (Steinmetz et al., 2018). Prominent among recent probes is the Neuropixels probe (Jun et al., 2017; Juavinett et al., 2019) (Figure 2), with a cross-section of 20 μm by 70 μm, about 50 times larger than that in our theoretical example (Figure 1A), and with electrodes on only one face. If we maintain the same filling-factor of Θ = 0.02, this suggests that Neuropixels probes can be placed as close as $2D$ = 165 μm and, for a λ_{AP} approximately 20 μm capture distance, record spikes from 0.01 to 0.02 of all neurons. The initial use of Neuropixels probes in mouse cortex yielded 0.6 to 1.0 neurons per site across 100 sites (Steinmetz et al., 2018), which is consistent with recording the majority of neurons within the capture distance of a single probe.

Considerations for Flexible Shanks

We shift our attention to electrodes with flexible shafts or, simply, soft wires. Though less mature than rigid electrodes, flexible electrodes have, in the ideal case, the advantage of bending with changes in local brain shape and size over the course of the day. This is essential for recording in flexible structures, like the hindbrain. Further, increasing evidence suggests that more flexible electrodes promote more stable neural interfaces (Xie et al., 2015; Fu et al., 2016; Luan et al., 2017; Yang et al., 2019). Flexible electrodes can be

Box 1. Dimensional estimates for a rigid electrode array.

- *What is the shank diameter required for insertion*? Standard formula for the threshold force, F, at the onset of buckling of a solid cylindrical beam (Timoshenko and Young, 1945) give

$$F = \left(\frac{\pi}{4}\right)^3 E \left(\frac{d_{shaft}^2}{L_{shaft}}\right)^2,$$

with the beam taken to be rigidly supported on one end. We equate F with F_i, approximated as $F_i \approx (F_0/d_0)\, d_{shaft}$, take E as the Young's modulus for diamond, and estimate a minimum diameter of $d_{shaft} = 4$ μm to insert a diamond shaft into cortex without the shaft buckling. A larger value may be required to penetrate the dura, recalling that $F \propto d_{shaft}^4$, and/or to accommodate sufficient numbers of electrode pads.

- What is the volume fraction of the brain occupied by the electrodes? Geometry sets this fraction at

$$\Theta = \frac{\pi}{8\sqrt{3}} \left(\frac{d_{shaft}}{D}\right)^2.$$

This fraction is $\Theta = 0.009$ for $d_{shaft} = 4$ μm and $\Theta \approx 0.02$ for $d_{shaft} = 6$ μm. The fraction must be small compared to the volume fraction of extracellular space, denoted α. Super-resolution imaging data from hippocampal slice shows that the fractional volume varies across anatomical locations (Tønnesen et al., 2018); it is $\alpha = 0.05$ in stratum pyramidalis, the cell layer, up in $\alpha = 0.36$ in fibrous regions, and has a mean value of $\overline{\alpha} = 0.19$. These values can change by 1.5-fold with neuromodulator concentration (Ding et al., 2016). Data from in vivo reports give similar values for $\overline{\alpha}$ (Syková and Nicholson, 2008).

- How many recording pads are required to cover the shank? The number of cells probed by one shank is

$$N = 2\sqrt{3}\, \rho\, D^2\, L_{shaft},$$

which yields $N = 280$. We set the number of recording pads equal to the target number of neurons to minimize, but not obviate, complications from spike sorting (Hill et al., 2011; Barnett et al., 2016). The surface of the shank is covered with one layer of lead wires, to bring signals to the surface of the brain. The overlaying layer is a mineral insulator, followed by a ground plane to shield the leads from the electrodes, and a second mineral insulator layer. The final, or fifth layer, contains the recording pads. Thru-holes connect each pad to the underlying wire (Figures 1B and 1C).

- *What is the size of the leads and pads*? We choose to wrap the leads for the N electrodes along the entire circumference of the first layer. We assume an equal lead width and separation distance of w_{lead}. This gives

$$w_{lead} = \frac{\pi d_{shaft}}{2N} = \frac{\pi}{4\sqrt{3}} \frac{1}{\rho D^2} \frac{d_{shaft}}{L_{shaft}},$$

which yields $w_{lead} = 35$ nm. Each electrode pad occupies an area with dimensions $\pi d_{shaft}/2 = 9$ μm wide by $2L_{shaft}/N = 14$ μm high, in which space remains for the inclusion of insulating gaps between pads. This corresponds to an area of $A_{pad} = 126$ μm^2.

driven into the brain with retractable support rods and thus provide a strategy to record in hindbrain, spinal cord, and even cortex where a rigid connection between the brain and the world is deleterious. As a matter of principle, the wires can be sufficiently fine to occupy a negligible volume fraction (Box 3).

We estimate that the same 280 electrode pads per shank target may be accommodated by a flexible rectangular shank with a 10 μm width and 1.5 μm thickness. Most estimates of the rigid probe (Boxes 1 and 2) apply to flexible shanks except for several points (Box 3).

Comparison with the State-of-the-Art Flexible Probes

The thinnest multi-channel flexible probes are currently fabricated with thicknesses of approximately 1 μm. To achieve the highest contact density, e-beam lithography is most promising for its approximately 10 nm spatial resolution (Luan et al., 2017; Wei et al., 2018; Yang et al., 2019) (Figure 3). This and related approaches (Chung et al., 2019) provide proof of the viability of flexible electrodes, although the demonstrated channel count per shank is about 20 times less than proposed array. In principle, the resolution of electron beam lithography should permit the fabrication process at a much higher electrode count but is limited by currently available back-end electronics.

It is also important to note that even brittle materials can be rendered flexible if they are sufficiently thin. Bending stiffness scales roughly with the cube of the film thickness. For the example of silicon, this allows a reduction in bending stiffness

Box 2. Electrical noise and shunting for a rigid electrode array.

● *How much thermal noise is generated by the recording pads*? There are two types of electrode interfaces, Faradaic and non-Faradaic, that transform electrical signals between the ionic conduction in solution and the electronic conduction in gold or other metals (Bard and Faulkner 2000). Non-Faradaic electrodes, also known as ideal polarizable electrodes, refer to interfaces for which no electrochemical, i.e., reduction-oxidation, reactions take place. Faradaic electrodes make use of reduction-oxidation processes at the extracellular solution-to-metal interface. Faradaic electrodes are characterized by a shot noise component that is associated with the electrochemical processes.

For electrophysiology, non-Faradaic electrodes are preferred. In this case, the electrical noise from the electrodes is solely thermal in origin and is associated primarily with resistances of the double-layer at the extracellular solution-to-metal interface, as well as any access resistances to the bulk electrolyte and tissue. Under the assumption that the resistance of the double-layer dominates the losses, the root-mean-square (RMS) thermal noise is

$$\delta V_{\text{pad}} = \sqrt{\frac{k_B T}{C_{\text{pad}}}},$$

which is derived by equating the noise energy $1/2\ C_{\text{pad}}\ \delta V_{\text{pad}}^2$ with the equipartition energy $1/2\ k_B T$, where k_B is the Boltzman constant and T is the temperature. A large electrode capacitance is clearly preferred based on noise considerations. The capacitance given by

$$C_{\text{pad}} = \epsilon_o \epsilon_{\text{double}} \frac{A_{\text{pad}}}{t_{\text{double}}}.$$

The double layer is characterized by a thickness $t_{\text{double}} = 0.3$ nm and relative dielectric constant $\epsilon_{\text{double}} = 2$ (Burak and Andelman, 2000), for which $C_{\text{pad}} = 7$ pF. The addition of a coating of titanium nitride (TiN) to the face of the electrode will dramatically increase the value of the surface area of the pad. The increase in area exceeds one hundred-fold at the onset on testing (Jun et al., 2017) and diminishes to a worst case of twenty-fold under chronic, in vivo recording conditions (T.D.H., unpublished data). Thus C_{pad} is conservatively replaced by $C_{\text{pad,TiN}} = 150$ pF and the estimated RMS noise is $\delta V_{\text{pad}} = 5.2\ \mu$V over the bandwidth associated with the double layer.

The noise will be reduced if the spectral bandwidth of the neuronal activity, f_{AP}, is less than the bandwidth, denoted f_{pad}, associated with the electrode and double layer. This bandwidth is found from input resistance between the neuron and the electrode times the capacitance, where the input resistance is estimated as the spreading resistance over the separation distance D, i.e.,

$$R_{\text{input}} = \frac{\rho_{brain}}{4\pi\overline{\alpha}D},$$

where we have corrected for the volume fraction, $\overline{\alpha}$ (Weissberg, 1963). The resistivity of cerebral spinal fluid in neocortex, denoted ρ_{brain}, is estimated to be in the range 2–4 Ωm (Logothetis et al., 2007). Thus $R_{\text{input}} \approx 60$ kΩ so that $f_{\text{pad}} = 1/2\pi R_{\text{input}} C_{\text{pad,TiN}} = 18$ kHz, or 4 times f_{AP}. Thus the filtered noise level will be $\delta V_{\text{pad}} = 5.2/\sqrt{18/10}\ \mu$V $= 4\ \mu$V.

● *How much thermal noise is generated by the leads to the recording pads*? The resistance of a gold, 35 nm thick by 35 nm wide wire is $R_{\text{lead}} = 30$ kΩ. The corresponding RMS thermal noise, also referred to as Johnson noise, is

$$\delta V_{\text{lead}} = \sqrt{4 k_B T R_{\text{lead}} f_{\text{AP}}}.$$

We estimate $\delta V_{\text{lead}} = 4\ \mu$V. The noise from the leads and electrode pads are, for our design, nominally equal.

● *What is the expected noise from passive tissue*? The electrode thermal noise must be compared with the variability in the extracellular signal that arises from background neuronal activity in cortex. The spreading resistance between a signal and a reference electrode spaced a distance Δd apart is $R_{\text{spreading}} = \rho_{brain}/4\pi\overline{\alpha}\Delta d$. The corresponding thermal noise is

$$\delta V_{\text{spreading}} = \sqrt{4 k_B T R_{\text{spreading}} f_{\text{AP}}}$$
$$= \sqrt{k_B T \frac{\rho_{brain}}{\pi\overline{\alpha}\Delta d} f_{\text{AP}}}.$$

For a reference spaced Δd =10 mm from the main electrodes, $\delta V_{\text{spreading}} = 130$ nV. This is negligible compared to the noise of the electrodes.

● *Is the capacitive coupling between electrodes leads deleterious*? The coupling between neighboring leads and leads and electrode pads can both attenuate and corrupt the measured signal. For our geometry (Figure 1B) and a fabrication plan with interposed short and long leads,

(Continued on next page)

Box 2. *Continued*

$$C_{\text{lead}} = \epsilon_o\ \epsilon_{\text{dielectric}} \frac{L_{\text{shaft}}}{2} w_{\text{lead}} \sum_{n=1}^{N} \frac{1}{\frac{d_{\text{shaft}}}{2} \text{cord}\left(2\pi \frac{n}{N}\right) - w_{\text{lead}}}$$

$$= \epsilon_o\ \epsilon_{\text{dielectric}} L_{\text{shaft}} \sum_{n=1}^{N/2} \frac{1}{\frac{2N}{\pi} \sin\left(\pi \frac{n}{N}\right) - 1},$$

where the sum accounts for coupling to all leads. The coupling between the leads and the pads is prevented by the incorporation of a ground plane with through-holes between the layer of pads and that of leads (Figure 1B).

We use $\epsilon_{\text{dielectric}} = 5$ for diamond and estimate $C_{\text{lead}} = 0.1$ pF. This value is negligible compared to both the capacitance of the pad and the capacitance of the gate of a field effect transistor at the input of an ultra-low noise amplifier (Wattanapanitch et al., 2007). The roll-off frequency for attenuation of high frequency components of the signal is $f_{3\text{dB}} = 1/(2\pi R_{\text{lead}} C_{\text{lead}}) = 5$ MHz for a lumped parameter model, or over two orders-of-magnitude larger than f_{AP}. Lastly, as a design rule, the expression for C_{lead} takes on a simple scaling in the limit of large N, i.e.,

$$\lim_{N \to \infty} C_{\text{lead}} \to \frac{\epsilon_o\ \epsilon_{\text{dielectric}} L_{\text{shaft}}}{2} \log_e\left(\frac{4}{\pi} N\right),$$

where 436.00 in Dwight (1961) was used.

- *What is the expected signal strength*? The signal strength from the electrode can be attenuated by the capacitance divider formed between the electrode capacitance and the input capacitance of the first-stage amplifier. Thus

$$\frac{\Delta V_{\text{meas}}}{\Delta V_{\text{cell}}} \approx \frac{C_{\text{pad,TiN}}}{C_{\text{pad,TiN}} + C_{\text{input}}}.$$

The input capacitance of an an ultra-low noise amplifier is less than 1 pF (Wattanapanitch et al., 2007). Thus $\Delta V_{\text{meas}}/\Delta V_{\text{cell}} \approx 1$. The maximum voltage for extracellular signals ranges from $\Delta V_{\text{cell}} = 300$ μV (Hill et al., 2011) to $\Delta V_{\text{cell}} = 1$ mV (Lemon, 1984), so a conservative upper bound is $\Delta V_{\text{meas}} < 300$ μV. High values of $C_{\text{pad,TiN}}$ values are clearly preferred to maximize the input signal as well as reduce thermal noise from the electrode.

from roughly 2 Nm for a standard 500 μm thick silicon to only 5 μNm for silicon thinned to a thickness of 12 μm. The resulting nearly six-order-of-magnitude increase in mechanical compliance allows many of the properties of more flexible materials to be achieved. For the particular case of silicon, this permits the design of flexible probes that incorporate electronics to be produced in state-of-the-art fabrication lines.

Interface Electronics and Power Limits

The signal from each electrode needs to be electronically buffered, i.e., transformed from a high impedance source to a low-impedance driver, amplified, and digitized. This task is performed by a field effect transistor placed at the top of the electrode. This transistor and the associated downstream amplification and digitization electronics will generate heat that must be dissipated in the air above the animal. The channel densities that we propose are high, i.e., $N/\sqrt{3}D^2 = 2.6 \times 10^5$ channels/mm^2 or twenty million channels across the readily accessible 8 mm by 10 mm cortical mantle in mice.

How much power can be safely dissipated? Recent studies on the suppression of neuronal activity by heating through the absorption of light (Owen et al., 2019) suggest that the threshold thermal load is roughly 0.06 W/mm^2; similar conclusions are found for light-induced vasodilation (Rungta et al., 2017). This is likely to be an underestimate as heating was local in these studies, yet it provides a guide and suggests the need for an electronic interface that dissipates less than 0.2 μW per channel. Recalling that thermal conduction by diamond is 30,000× that of air, essentially all of the heat will flow into the brain unless steps are taken to block this flow. For example, a gap between the electrode and the electronics that is comprised of epoxy-silica should reduce the conduction of heat into the brain by a factor of 0.4.

Feasibility of Ultra-low Power Amplification

Amplifiers for neuronal recording whose power dissipation is close to the fundamental physical limits set by input-referred thermal noise in transistors have already been built (Wattanapanitch et al., 2007; Sarpeshkar 2010; Wattanapanitch and Sarpeshkar, 2011). Such amplifiers have a power dissipation that is inversely proportional to the square of the input-referred noise as well as linear in the required bandwidth; 22.8 in Sarpeshkar (2010). A relevant design was configured for an input-referred noise of 3.1 μV RMS and a 5.3 kHz bandwidth and realized with a gain of nearly 100, an input capacitance significantly less than 1 pF, and a "1/f" noise that is negligible for spike recording. The concomitant measured dissipation was 7.6 μW per channel.

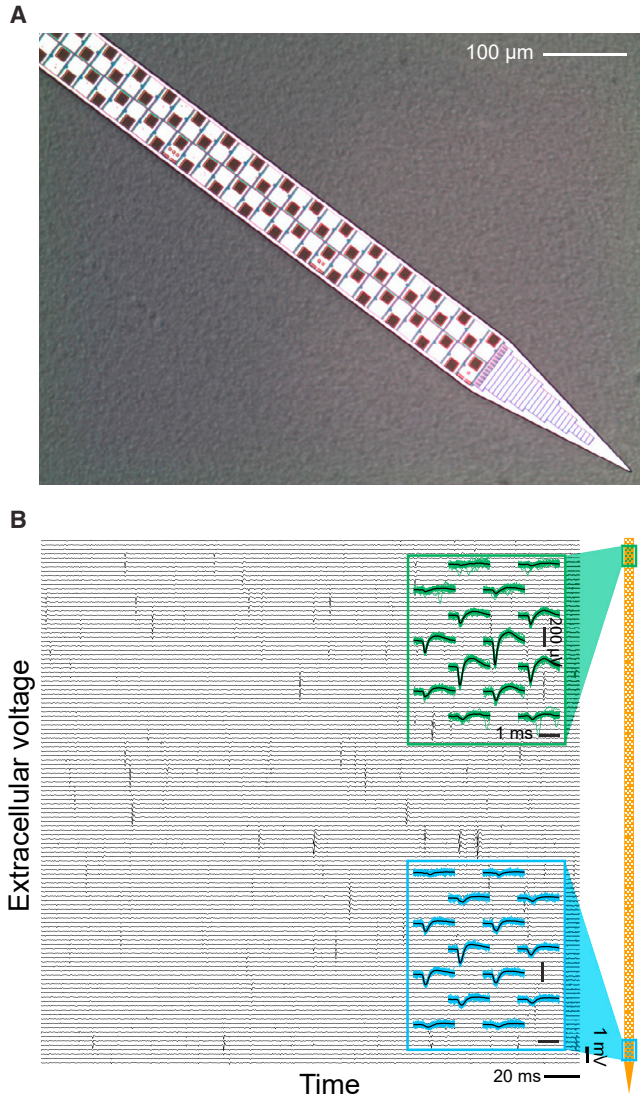

Figure 2. A State-of-the-Art Rigid Probe

(A) Photograph of the distal 68 sites of the 960 sites on a shank of a Neuropixels probe. The shank is 10 mm long, 70 μm wide, and 24 μm thick, with 12 μm by 12 μm TiN-coated recording sites pitched at 2 per 20 μm of shank length.

(B) Two example recordings from Neuropixels probe pads. The probe was chronically implanted in rat prefrontal cortex one day prior to data acquisition. Blue traces and green traces are 30 raw traces in the vicinity of a spike near the top (green) and bottom (blue) of the probe; black lines are average of those traces. Adapted from Jun et al. (2017).

This implies a dissipation of 7.6 μW × (3.1 μV/ 6 μV)^2 × (10 kHz/5.3 kHz) = 3.8 μW per channel, or 1.5 W/mm^2, using the 6 μV RMS noise floor of our electrodes. This value, however, exceeds the target value for power dissipation.

A novel technique known as adaptive power biasing permits the power dissipation of a large, multi-channel electrode to be reduced by over an order of magnitude (Sarpeshkar 2010; Wattanapanitch and Sarpeshkar, 2011). The statistics of multi-channel arrays are such that their input-referred noise varies over a probability distribution. Thus one low-noise amplifier can measure, calibrate, digitally store, and bias all other amplifiers in a multi-channel system such that each channel only dissipates power that is appropriate to the noise floor of the associated electrode pad. The method is effective because the mean power dissipation of an amplifier in a multi-channel array, which is inversely proportional to the square of the input-referred noise, is significantly lower than that of an array of amplifiers designed for a fixed input noise; e.g., our estimated mean RMS noise floor of 6 μV. Thus, for our electrode array, we estimate that we could dissipate less than 0.15 W/mm^2, on average. This value is less than the target value for power dissipation, and thus supports the feasibility of our approach.

Additional decrements on power dissipation can occur by increasing the acceptable noise floor toward the value with background activity, i.e., δV = 25 μV, mindful of the quadratic decrement in power dissipation with increasing amplifier noise. Further improvements may also be achieved with lower supply voltages and, as in the case of Neuropixels probes (Jun et al., 2017), by disabling unused channels.

Digitization

What of the power costs of digitization? Electronics with adaptive or programmable gain and analog-to-digital converters (ADCs) can provide a large dynamic range of operation, i.e., peak signal relative to noise, and good bit precision while maintaining low power dissipation. As an example (Wattanapanitch and Sarpeshkar, 2011), capacitively coupled ADCs with programmable gain can readily digitize amplified action potentials that range in amplitude from 10 μV, i.e., at the noise floor and thus amplified with the highest gain, to 3 mV, i.e., amplified with the lowest gain, with 8-bit precision over a 12-bit dynamic range. Well-known techniques for ultra-low power subthreshold digital design can ensure that switching power dissipation is minimized, so that the predominant power dissipation originates from the electrode amplifiers and not the ADCs (Sarpeshkar, 2010).

A final point is data transmission. The bit rate per square millimeter for 8-bits of digitization depth and f_{AP} = 10 kHz is $2f_{AP}N/(\sqrt{3}D^2)\times 8 = 65$ GHz. From all of cortex, the rate is about 5 THz. This is well within the capacity of a single fiber optic transmission line (Stark et al., 2001). Nonetheless, one may wish to transmit only segments of the data with potential spikes. Each action potential will contribute to multiple electrode pads, so that the detection of action potentials is a source localization problem. The fraction of active electrodes at a given time can be estimated for the case of asynchronous activity and action potentials that contribute to a subset, denoted n, of the electrodes on a shank, where each spike occurs at an average rate of r and lasts for Δt. The fraction of time that an electrode is active is then p = $1-(1-r\Delta t)^n$; we assume a spread of ±100 μm (Figure 2), implying n = 14 for a 14 μm pitch (Figure 1C), and take Δt = 2 ms and r = 10/s. We find p = 0.25, implying that the bit rate per square millimeter can drop to 16 GHz and that the bit rate for the cortical mantle drops to nearly 1 THz. The data rate can be reduced further with optimized compression schemes.

Box 3. Estimates for a flexible electrode array

- *What is the minimal thickness of a flexible probe*? While mineral-based materials work as insulators for rigid shanks, they can easily crack on a flexible shank. Polymers are typically used as insulators for flexible probes and a thickness of approximately 500 nm is typically required. Taking d_{lead} = 40 nm, 300 leads can readily fit in two 10 μm wide lead layers and three insulator layers, yielding an overall thickness of 1.5 μm and cross-sectional area of 15 μm^2 (Figure 3A).
- *What is the shuttle diameter required for insertion*? The shuttle should have a cross section similar to that of the rigid probe (Felix et al., 2013; Zhao et al., 2019) (Box 1), i.e., 6 μm diameter for diamond.
- *How should the array be transiently attached the shuttle for insertion*? Temporarily attaching the flexible probe to the shuttle can be achieved with geometrical anchors (Luan et al., 2017) or water-soluble adhesives (Felix et al., 2013; Zhao et al., 2019).
- *What is the tissue displacement*? The total displacement for the flexible probe is half of that for the rigid probe, or Θ = 0.01. The shuttle will transiently triple the volume occupied by the flexible electrode alone. Yet this increase in negligible if the shanks are inserted sequentially. On the other hand, there is potential for tissue damage during the process of insertion per se (Na et al., 2019; Zhao et al., 2019; Ferro et al. 2018; Joo et al 2019).

Biomechanics of Probe Insertion

Mechanical compression of the brain during the insertion of either rigid or flexible shanks could pose complications. First, it is simply unknown if neocortex can be compressed to 0.98 of its original volume. This presumably can occur given the ability of the brain to accommodate tumors of roughly 0.1 times the cortical volume before there are clinical indicators (Jalali et al., 2010). It is entirely possible that the compression would lead solely to changes in the volume of ventricles. Second, even if the brain can perform normally in a reduced volume, the act of inserting electrodes can lead to dysfunction from the compression of the pia and upper layers of cortex during insertion. Established procedures may obviate this issue, such as the use of a weak vacuum to stabilize the surface of the brain onto a mesh of guide tubes (Venkatachalam et al., 1999) and vibro-cutting of the dura and pia (Gilleland et al., 2015). Other factors should be considered as well, particularly the insertion speed (Rousche and Normann, 1992; Maynard et al., 1997; Nicolelis et al., 2003; Rennaker et al., 2005; Felix et al., 2013) and possible enzymatic treatment of the pia (Paralikar and Clement, 2008).

The vasculature could pose challenges in gaining access to all locations, as the pial surface of cortex is covered with venules and arterioles. These two classes of vessels overlap with each other but not within a class. Together, they roughly cover 0.1 of the surface of mouse cortex. It may be possible to penetrate through vessels with a sharp tip at the end of the shank and have the vessel seal; such tests remain unreported. While sparse blockage to surface arterioles is tolerated, blockage of a penetrating vessel will lead to an approximately 500 μm diameter infarct (Shih et al., 2013). A second issue is the potential lesioning of microvessels (Bohm et al., 2019), which in mice occupy close to 0.01 of the cortical volume, have mean diameter of 2.5 μm, and have no directional bias (Blinder et al., 2013). We reanalyzed published data (Blinder et al., 2013) and estimate that the probability of encountering a microvessel varies as $1-e^{-z/z_o}$ with insertion depth, z, and z_o = 300 μm. Nonetheless, it is likely, based on experience with silicon shaft electrodes, that microvessels splay and are spared from damage with a slowly inserted shaft. Further, sparse blockage of microvessels is tolerated (Shih et al., 2013).

DISCUSSION

The essence of our analysis is that basic physical estimates suggest the utility of moving toward a program of all-cortex, if not all-brain, spike-based electrical imaging through the adoption of non-traditional materials and the extension of current fabrication processes. Practical limits exist in terms of fabrication processes. For example, one can only pull a wire to be so thin, or only so reliably deposit a layer of insulation above a minimum thickness. Economics will limit the choice of materials. Electronic heating and power considerations, while likely to be challenging, do not appear to be insurmountable with respect to fundamental limits. All told, our analysis points to the adoption of an engineering-based feasibility study for rigid electrodes.

Soft electrodes represent an emerging technology (Xie et al., 2015; Luan et al., 2017; Zhao et al., 2017; Chung et al., 2019). Beyond issues of scientific investigation, particularly in subcortical regions, they may have extensive utility in brain-machine interfaces that involve the brainstem and spinal cord. Our analysis points to the adoption of a discovery-based program to explore soft materials for flexible electrodes.

Epilog

The practical problems that must be overcome for electrode technology to reach its full potential appear daunting but can be addressed and likely surmounted. The insertion of a dense array of shanks, one shank every 40 μm, will pose significant challenges, as the pitch is one tenth that of the "Utah" array (Maynard et al., 1997) (Blackrock Microsystems). Signal processing at the head of the shank will definitely be required. Automation for craniotomies (Jeong et al., 2012) and automated shank insertion will likely be required. The vasculature will likely occupy some of the space assumed for this array of shanks. Lastly, while spikes appear to be the major currency of neuronal computation, the brain-wide measurement and understanding of subcellular electrodynamics, certainly down to the level of fine dendrites (Häusser et al., 2000; Moore et al., 2017;

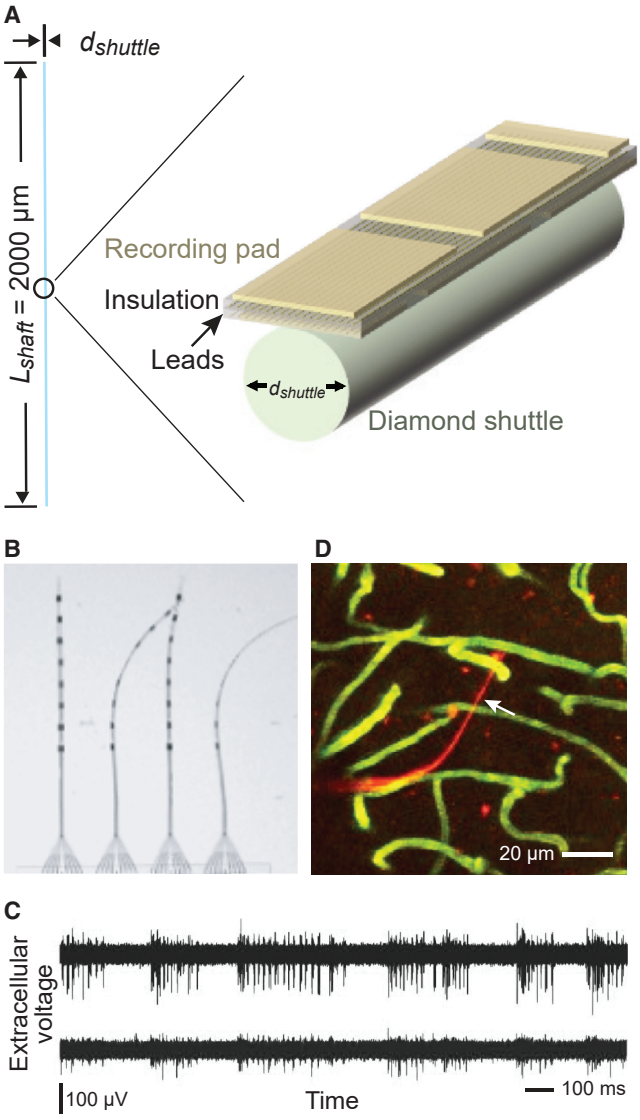

Figure 3. Flexible Probes

(A) A proposed probe is constructed of gold pads and epoxy insulators. A diamond shank provides temporary rigidity for insertion.

(B) A state-of-the-art flexible multi-channel neural probe fabricated by electron beam lithography, with a shank width of 8 µm, thickness of 0.8 µm, and electrode pad size of 5 µm by 15 µm.

(C) Representative electrical traces from the probe in (B).

(D) Three-dimensional reconstruction of vasculature by *in vivo* two-photon microscopy (Kleinfeld et al., 1998) around a probe (red). Data obtained two months after implantation and shown as a maximum projection 100,320 µm below the pia. Adapted from Wei et al. (2018).

Ranganathan et al., 2018), represents an important albeit futuristic goal.

ACKNOWLEDGMENTS

These investigations were initiated in response to the National Science Foundation workshop on "Physical, Engineering and Biological Limits to Brain Measurements" in 2014 and a related workshop at the HHMI Janelia Research Campus in 2017. We thank X. Ji for help with the analysis of the vasculature, D.P. Arovas, G.E. Blonder, T.J. Gardner and U.V. Nägerl for discussions, and B. Friedman for critique of an early version of the manuscript. This work was supported by the Cold Spring Harbor Laboratory Crick-Clay Professorship, the Howard Hughes Medical Institute, NEI grant EY028397, NHLBI grant HL140153, NINDS grants NS107466, NS109361, and NS0905905, and ONR grant N00014-19-1-2434.

AUTHOR CONTRIBUTIONS

T.D.H. and D.K. wrote the manuscript with input from all authors, and D.K. performed the calculations presented in Boxes 1 and 2, with critique from all authors.

DECLARATION OF INTERESTS

The authors declare no competing interests.

Received: March 31, 2019
Revised: June 30, 2019
Accepted: August 3, 2019
Published: September 5, 2019

REFERENCES

Abdelfattah, A.S., Kawashima, T., Singh, A., Novak, O., Liu, H., Shuai, Y., Huang, Y.-C., Campagnola, L., Seeman, S.C., Yu, J., et al. (2019). Bright and photostable chemigenetic indicators for extended in vivo voltage imaging. Science *364*, 699–704.

Adam, Y., Kim, J.J., Lou, S., Zhao, Y., Brinks, D., Wu, H., Mostajo-Radji, M.A., Kheifets, S., Parot, V., Chettih, S., et al. (2019). Voltage imaging and optogenetics reveal behaviour-dependent changes in hippocampal dynamics. Nature *569*, 413–417.

Alivisatos, A.P., Chun, M., Church, G.M., Greenspan, R.J., Roukes, M.L., and Yuste, R. (2012). The brain activity map project and the challenge of functional connectomics. Neuron *74*, 970–974.

Bard, A.J., and Faulkner, L.R. (2000). Electrochemical Methods: Fundamentals and Applications, Second Edition (New York: Wiley Press).

Barnett, A.H., Magland, J.F., and Greengard, L.F. (2016). Validation of neural spike sorting algorithms without ground-truth information. J. Neurosci. Methods *264*, 65–77.

Blinder, P., Tsai, P.S., Kaufhold, J.P., Knutsen, P.M., Suhl, H., and Kleinfeld, D. (2013). The cortical angiome: an interconnected vascular network with noncolumnar patterns of blood flow. Nat. Neurosci. *16*, 889–897.

Bohm, T., Joseph, K., Kirsch, M., Moroni, R., Hilger, A., Osenberg, M., Manke, I., Johnson, M., Stieglitz, T., Hofmann, U.G., et al. (2019). Quantitative synchrotron X-ray tomography of the material-tissue interface in rat cortex implanted with neural probes. Sci. Rep. *9*, 7646, https://doi.org/10.1038/s41598-019-42544-9.

Burak, Y., and Andelman, D. (2000). Hydration interactions: aqueous solvent effects in electric double layers. Phys. Rev. E *62*, 5295–5312.

Buzsáki, G. (2004). Large-scale recording of neuronal ensembles. Nat. Neurosci. *7*, 446–451.

Buzsáki, G., Stark, E., Berényi, A., Khodagholy, D., Kipke, D.R., Yoon, E., and Wise, K.D. (2015). Tools for probing local circuits: high-density silicon probes combined with optogenetics. Neuron *86*, 92–105.

Charkhkar, H., Knaack, G.L., McHail, D.G., Mandal, H.S., Peixoto, N., Rubinson, J.F., Dumas, T.C., and Pancrazio, J.J. (2016). Chronic intracortical neural recordings using microelectrode arrays coated with PEDOT-TFB. Acta Biomater. *32*, 57–67.

Chung, J.E., Joo, H.R., Fan, J.L., Liu, D.F., Barnett, A.H., Chen, S., Geaghan-Breiner, C., Karlsson, M.P., Karlsson, M., Lee, K.Y., et al. (2019). High-density, long-lasting, and multi-region electrophysiological recordings using polymer electrode arrays. Neuron *101*, 21–31.e5.

Denk, W., and Horstmann, H. (2004). Serial block-face scanning electron microscopy to reconstruct three-dimensional tissue nanostructure. PLoS Biol. *2*, e329.

Ding, F., O'Donnell, J., Xu, Q., Kang, N., Goldman, N., and Nedergaard, M. (2016). Changes in the composition of brain interstitial ions control the sleep-wake cycle. Science *352*, 550–555.

Dwight, H.B. (1961). Tables on Integrals ad Other Mathematical Data, Fourth Edition (NY: The Macmillian Company).

Fee, M.S., Mitra, P.P., and Kleinfeld, D. (1996). Variability of extracellular spike waveforms of cortical neurons. J. Neurophysiol. *76*, 3823–3833.

Felix, S.H., Shah, K.G., Tolosa, V.M., Sheth, H.J., Tooker, A.C., Delima, T.L., Jadhav, S.P., Frank, L.M., and Pannu, S.S. (2013). Insertion of flexible neural probes using rigid stiffeners attached with biodissolvable adhesive. J. Vis. Exp. *79*, e50609.

Ferro, M.D., Proctor, C.M., Gonzalez, A., Zhao, E., Slezia, A., Pas, J., Dijk, G., Donahue, M.J., Williamson, A., Malliaras, G.G., et al. (2018). NeuroRoots, a bio-inspired, seamless Brain Machine Interface device for long-term recording. bioRxiv. https://doi.org/10.1101/460949.

Fu, T.-M., Hong, G., Zhou, T., Schuhmann, T.G., Viveros, R.D., and Lieber, C.M. (2016). Stable long-term chronic brain mapping at the single-neuron level. Nat. Methods *13*, 875–882.

Ganguli, S., and Sompolinsky, H. (2012). Compressed sensing, sparsity, and dimensionality in neuronal information processing and data analysis. Annu. Rev. Neurosci. *35*, 485–508.

Gao, P., Trautmann, E., Yu, B., Santhanam, G., Ryu, S., Shenoy, K., and Ganguli, S. (2017). A theory of multineuronal dimensionality, dynamics and measurement. bioRxiv. https://doi.org/10.1101/214262.

Gilleland, C.L., Falls, A.T., Noraky, J., Heiman, M.G., and Yanik, M.F. (2015). Computer-assisted transgenesis of caenorhabditis elegans for deep phenotyping. Genetics *201*, 39–46.

Grienberger, C., and Konnerth, A. (2012). Imaging calcium in neurons. Neuron *73*, 862–885.

Häusser, M., Spruston, N., and Stuart, G.J. (2000). Diversity and dynamics of dendritic signaling. Science *290*, 739–744.

Hayworth, K.J., Peale, D., Januszewski, M., Knott, G.W., Lu, Z., Xu, C.S., and Hess, H.F. (2019). GCIB-SEM: A path to 10 nm isotropic imaging of cubic millimeter volumes. bioRxiv. https://doi.org/10.1101/563239.

Hill, D.N., Mehta, S.B., and Kleinfeld, D. (2011). Quality metrics to accompany spike sorting of extracellular signals. J. Neurosci. *31*, 8699–8705.

Jack, J.J.B., Noble, D., and Tsien, R.W. (1974). Electric Current Flow in Excitable Cells (Oxford: Clarendon press).

Jalali, R., Mallick, I., Dutta, D., Goswami, S., Gupta, T., Munshi, A., Deshpande, D., and Sarin, R. (2010). Factors influencing neurocognitive outcomes in young patients with benign and low-grade brain tumors treated with stereotactic conformal radiotherapy. Int. J. Radiat. Oncol. Biol. Phys. *77*, 974–979.

Jeong, D.C., Tsai, P.S., and Kleinfeld, D. (2012). Prospect for feedback guided surgery with ultra-short pulsed laser light. Curr. Opin. Neurobiol. *22*, 24–33.

Ji, N. (2017). Adaptive optical fluorescence microscopy. Nat. Methods *14*, 374–380.

Joo, H.R., Fan, J.L., Chen, S., Pebbles, J.A., Liang, H., Chung, J.E., Yorita, A.M., Tooker, A., Tolosa, V., Geaghan-Breiner, C., et al. (2019). A microfabricated, 3D-sharpened silicon shuttle for insertion of flexible electrode arrays through dura mater into brain. J. Neural Eng. https://doi.org/10.1088/1741-2552/ab2b2e.

Juavinett, A.L., Bukheet, G., and Churchland, A.K. (2019). Chronically-implanted Neuropixels probes enable high yield recordings in freely moving mice. eLife *8*, e47188, https://doi.org/10.7554/eLife.47188.

Jun, J.J., Steinmetz, N.A., Siegle, J.H., Denman, D.J., Bauza, M., Barbarits, B., Lee, A.K., Anastassiou, C.A., Andrei, A., Aydın, Ç., et al. (2017). Fully integrated silicon probes for high-density recording of neural activity. Nature *551*, 232–236.

Kasthuri, N., Hayworth, K.J., Berger, D.R., Schalek, R.L., Conchello, J.A., Knowles-Barley, S., Lee, D., Vázquez-Reina, A., Kaynig, V., Jones, T.R., et al. (2015). Saturated reconstruction of a volume of neocortex. Cell *162*, 648–661.

Kleinfeld, D., Mitra, P.P., Helmchen, F., and Denk, W. (1998). Fluctuations and stimulus-induced changes in blood flow observed in individual capillaries in layers 2 through 4 of rat neocortex. Proc. Natl. Acad. Sci. USA *95*, 15741–15746.

Kleinfeld, D., Bharioke, A., Blinder, P., Bock, D.D., Briggman, K.L., Chklovskii, D.B., Denk, W., Helmstaedter, M., Kaufhold, J.P., Lee, W.C., et al. (2011). Large-scale automated histology in the pursuit of connectomes. J. Neurosci. *31*, 16125–16138.

Knott, G., Marchman, H., Wall, D., and Lich, B. (2008). Serial section scanning electron microscopy of adult brain tissue using focused ion beam milling. J. Neurosci. *28*, 2959–2964.

Knutsen, P.M., Mateo, C., and Kleinfeld, D. (2016). Precision mapping of the vibrissa representation within murine primary somatosensory cortex. Philos. Trans. R. Soc. Lond. B Biol. Sci. *371*, e20150351.

Kornfeld, J., and Denk, W. (2018). Progress and remaining challenges in high-throughput volume electron microscopy. Curr. Opin. Neurobiol. *50*, 261–267.

Lehky, S.R., Kiani, R., Esteky, H., and Tanaka, K. (2014). Dimensionality of object representations in monkey inferotemporal cortex. Neural Comput. *26*, 2135–2162.

Lemon, R. (1984). Methods for Neuronal Recording in Conscious Animals (Chichester: John Wiley and Sons).

Liu, R., Li, Z., Marvin, J.S., and Kleinfeld, D. (2019). Direct wavefront sensing enables functional imaging of infragranular axons and spines. Nat. Methods *16*, 615–618.

Logothetis, N.K., Kayser, C., and Oeltermann, A. (2007). In vivo measurement of cortical impedance spectrum in monkeys: implications for signal propagation. Neuron *55*, 809–823.

Luan, L., Wei, X., Zhao, Z., Siegel, J.J., Potnis, O., Tuppen, C.A., Lin, S., Kazmi, S., Fowler, R.A., Holloway, S., et al. (2017). Ultraflexible nanoelectronic probes form reliable, glial scar-free neural integration. Sci. Adv. *3*, e1601966.

Ludwig, K.A., Langhals, N.B., Joseph, M.D., Richardson-Burns, S.M., Hendricks, J.L., and Kipke, D.R. (2011). PEDOT polymer coatings facilitate smaller neural recording electrodes. Journal of Neural Engineering *8*, e014001.

Maynard, E.M., Nordhausen, C.T., and Normann, R.A. (1997). The Utah intracortical electrode array: A recording structure for potential brain-computer interfaces. Electroencephalogr. Clin. Neurophysiol. *102*, 228–239.

Moore, J.J., Ravassard, P.M., Ho, D., Acharya, L., Kees, A.L., Vuong, C., and Mehta, M.R. (2017). Dynamics of cortical dendritic membrane potential and spikes in freely behaving rats. Science *355*, eaaj1497.

Na, K., Sperry, Z.J., Lu, J., Voeroeslakos, M., Parizi, S.S., Bruns, T.M., Yoon, E., and Seymour, J.P. (2019). Novel diamond shuttle to deliver flexible bioelectronics with reduced tissue compression. bioRxiv. https://doi.org/10.1101/435800.

Naundorf, B., Wolf, F., and Volgushev, M. (2006). Unique features of action potential initiation in cortical neurons. Nature *440*, 1060–1063.

Negi, S., Bhandari, R., Rieth, L., and Solzbacher, F. (2010). In vitro comparison of sputtered iridium oxide and platinum-coated neural implantable microelectrode arrays. Biomed. Mater. *5*, 15007.

Nicolelis, M.A.L., Dimitrov, D., Carmena, J.M., Crist, R., Lehew, G., Kralik, J.D., and Wise, S.P. (2003). Chronic, multisite, multielectrode recordings in macaque monkeys. Proc. Natl. Acad. Sci. USA *100*, 11041–11046.

Obaid, A., Wu, Y.-W., Hanna, M., Nix, W., Ding, J., and Melosh, N. (2018). Ultra-sensitive measurement of brain penetration with microscale probes for brain machine interface considerations. bioRxiv. https://doi.org/10.1101/454520.

Owen, S.F., Liu, M.H., and Kreitzer, A.C. (2019). Thermal constraints on in vivo optogenetic manipulations. Nat. Neurosci. *22*, 1061–1065.

Paralikar, K.J., and Clement, R.S. (2008). Collagenase-aided intracortical microelectrode array insertion: effects on insertion force and recording performance. IEEE Trans. Biomed. Eng. *55*, 2258–2267.

Petersen, C.C. (2007). The functional organization of the barrel cortex. Neuron *56*, 339–355.

Platisa, J., and Pieribone, V.A. (2018). Genetically encoded fluorescent voltage indicators: are we there yet? Curr. Opin. Neurobiol. *50*, 146–153.

Plaza, S.M., Scheffer, L.K., and Chklovskii, D.B. (2014). Toward large-scale connectome reconstructions. Curr. Opin. Neurobiol. *25*, 201–210.

Ranganathan, G.N., Apostolides, P.F., Harnett, M.T., Xu, N.L., Druckmann, S., and Magee, J.C. (2018). Active dendritic integration and mixed neocortical network representations during an adaptive sensing behavior. Nat. Neurosci. *21*, 1583–1590.

Reitboeck, H.J. (1983). Fiber microelectrodes for electrophysiological recordings. J. Neurosci. Methods *8*, 249–262.

Rennaker, R.L., Street, S., Ruyle, A.M., and Sloan, A.M. (2005). A comparison of chronic multi-channel cortical implantation techniques: manual versus mechanical insertion. J. Neurosci. Methods *142*, 169–176.

Rivnay, J., Leleux, P., Ferro, M., Sessolo, M., Williamson, A., Koutsouras, D.A., Khodagholy, D., Ramuz, M., Strakosas, X., Owens, R.M., et al. (2015). High-performance transistors for bioelectronics through tuning of channel thickness. Sci. Adv. *1*, e1400251.

Rousche, P.J., and Normann, R.A. (1992). A method for pneumatically inserting an array of penetrating electrodes into cortical tissue. Ann. Biomed. Eng. *20*, 413–422.

Rubinov, M., Ypma, R.J.F., Watson, C., and Bullmore, E.T. (2015). Wiring cost and topological participation of the mouse brain connectome. Proc. Natl. Acad. Sci. USA *112*, 10032–10037.

Rungta, R.L., Osmanski, B.-F., Boido, D., Tanter, M., and Charpak, S. (2017). Light controls cerebral blood flow in naive animals. Nat. Commun. *8*, 14191.

Sarpeshkar, R. (2010). Ultra Low Power Bioelectronics: Fundamentals, Biomedical Applications, and Biol.-inspired Systems (Cambridge, UK: Cambridge University Press).

Schölvinck, M.L., Saleem, A.B., Benucci, A., Harris, K.D., and Carandini, M. (2015). Cortical state determines global variability and correlations in visual cortex. J. Neurosci. *35*, 170–178.

Shih, A.Y., Blinder, P., Tsai, P.S., Friedman, B., Stanley, G., Lyden, P.D., and Kleinfeld, D. (2013). The smallest stroke: occlusion of one penetrating vessel leads to infarction and a cognitive deficit. Nat. Neurosci. *16*, 55–63.

Stark, J.B., Mitra, P.P., and Sengupta, A. (2001). Capacity of nonlinear wavelength division multiplexing fiber optic transmission line. Optical Fiber Technology *7*, e275288.

Steinmetz, N.A., Koch, C., Harris, K.D., and Carandini, M. (2018). Challenges and opportunities for large-scale electrophysiology with Neuropixels probes. Curr. Opin. Neurobiol. *50*, 92–100.

Stringer, C., Pachitariu, M., Steinmetz, N., Carandini, M., and Harris, K.D. (2019). High-dimensional geometry of population responses in visual cortex. Nature *571*, 361–365.

Syková, E., and Nicholson, C. (2008). Diffusion in brain extracellular space. Physiol. Rev. *88*, 1277–1340.

Theis, L., Berens, P., Froudarakis, E., Reimer, J., Román Rosón, M., Baden, T., Euler, T., Tolias, A.S., and Bethge, M. (2016). Benchmarking spike rate inference in population calcium imaging. Neuron *90*, 471–482.

Timoshenko, S., and Young, D.H. (1945). Theory of Structures (New York: McGraw Hill Book Company).

Tønnesen, J., Inavalli, V.V.G.K., and Nägerl, U.V. (2018). Super-resolution imaging of the extracellular space in living brain tissue. Cell *172*, 1108–1121.e15.

Tsai, P.S., Kaufhold, J.P., Blinder, P., Friedman, B., Drew, P.J., Karten, H.J., Lyden, P.D., and Kleinfeld, D. (2009). Correlations of neuronal and microvascular densities in murine cortex revealed by direct counting and colocalization of nuclei and vessels. J. Neurosci. *29*, 14553–14570.

Venkatachalam, S., Fee, M.S., and Kleinfeld, D. (1999). Ultra-miniature headstage with 6-channel drive and vacuum-assisted micro-wire implantation for chronic recording from the neocortex. J. Neurosci. Methods *90*, 37–46.

Vitale, F., Vercosa, D.G., Rodriguez, A.V., Pamulapati, S.S., Seibt, F., Lewis, E., Yan, J.S., Badhiwala, K., Adnan, M., Royer-Carfagni, G., et al. (2018). Fluidic microactuation of flexible electrodes for neural recording. Nano Lett. *18*, 326–335.

Wattanapanitch, W., and Sarpeshkar, R. (2011). A low-power 32-channel digitally programmable neural recording integrated circuit. IEEE Trans. Biomed. Circuits Syst. *5*, 592–602.

Wattanapanitch, W., Fee, M., and Sarpeshkar, R. (2007). An energy-efficient micropower neural recording amplifier. IEEE Trans. Biomed. Circuits Syst. *1*, 136–147.

Wei, X., Luan, L., Zhao, Z., Li, X., Zhu, H., Potnis, O., and Xie, C. (2018). Nanofabricated ultraflexible electrode arrays for high-density intracortical recording. Adv Sci (Weinh) *5*, 1700625.

Weissberg, H.L. (1963). Effective diffusion coefficient in porous media. J. Appl. Phys. *34*, 2636–2640.

Weltman, A., Yoo, J., and Meng, E. (2016). Flexible, penetrating brain probes enabled by advances in polymer microfabrication. Micromachines (Basel) *7*, e180.

Whalen, J.J., III, Young, J., Weiland, J.D., and Searsonb, J.C. (2006). Electrochemical characterization of charge injection at electrodeposited platinum electrodes in phosphate buffered saline. J. Electrochem. Soc. *153*, C834–C839.

Xie, C., Liu, J., Fu, T.-M., Dai, X., Zhou, W., and Lieber, C.M. (2015). Three-dimensional macroporous nanoelectronic networks as minimally invasive brain probes. Nat. Mater. *14*, 1286–1292.

Yang, X., Zhou, T., Zwang, T.J., Hong, G., Zhao, Y., Viveros, R.D., Fu, T.-M., Gao, T., and Lieber, C.M. (2019). Bioinspired neuron-like electronics. Nat. Mater. *18*, 510–517.

Zhao, Z., Luan, L., Wei, X., Zhu, H., Li, X., Lin, S., Siegel, J.J., Chitwood, R.A., and Xie, C. (2017). Nanoelectronic coating enabled versatile multifunctional neural probes. Nano Lett. *17*, 4588–4595.

Zhao, Z., Li, X., He, F., Wei, X., Lin, S., and Xie, C. (2019). Parallel, minimally-invasive implantation of ultra-flexible neural electrode arrays. J. Neural Eng. *16*, 035001.